Wall-modeled LES of the Gaussian bump using the POD-mode-augmented wall model

By C. Hansen†, X. I. A. Yang‡, M. Abkar† AND P. Moin

1. Motivation and objectives

The strict near-wall grid resolution requirements at high Reynolds numbers make wall modeling a necessity for large-eddy simulations (LES) (Choi & Moin 2012; Yang & Griffin 2021). The basic concept of wall-modeled LES (WMLES) is shown in schematic form in Figure 1(a). As the LES grid in WMLES is coarse and scales with the boundary-layer thickness, the wall shear stress and wall-heat flux cannot be computed per the discretization scheme. Instead, a wall model is employed. It takes LES information in the wall-adjacent cell(s) and computes the wall shear stress and wall-heat flux, which are then used to close the LES governing equations at the wall.

The most commonly employed class of wall models is the equilibrium wall model (EWM) (Schumann 1975; Bou-Zeid *et al.* 2005; Kawai & Larsson 2012; De Vanna *et al.* 2021). The algebraic variant of EWM computes the wall fluxes according to some mean flow scaling in the wall-adjacent computational cell(s) which is usually taken as the law of the wall (LoW). The mean flow scaling is matched with the LES velocity at an off-wall location locally and instantaneously, resulting in algebraic equations for the friction velocity and wall temperature. The wall fluxes are then computed based on these quantities. Another popular variant of EWM is based on solving the thin boundary-layer equations (TBLEs). In these models, only the Reynolds stress term and the viscous stress term are retained in the TBLEs, and the Reynolds stress term is closed using a zero-equation eddy viscosity model (Kawai & Larsson 2012; Yang & Lv 2018; Chen *et al.* 2022). The resulting ordinary differential equations (ODEs) are then solved on a 1D fine near-wall grid with the off-wall boundary condition provided by matching with the LES in the wall-adjacent cell(s). The wall fluxes can then be calculated from the ODE solutions on the wall model grid.

Although the EWMs discussed above have much in their favor regarding simplicity, model stability, and a low computational cost, it has long been known that EWMs struggle in non-equilibrium flows, and thus, improvements in wall modeling beyond the EWMs have been attempted (Piomelli & Balaras 2002; Larsson *et al.* 2016; Bose & Park 2018). One approach is based on solving the full TBLEs with all of the non-equilibrium terms included (Park & Moin 2014). This method, however, comes at the cost of solving a full set of partial differential equations, which often adds a 100% overhead to the LES as in Park & Moin (2016). Approaches that account for non-equilibrium effects at a lower computational cost are the integral wall model by Yang *et al.* (2015) and the Lagrangian relaxation toward equilibrium wall model by Fowler *et al.* (2022). Both models perform wall-normal integration of the full TBLEs with an assumed analytical form for the LES-grid filtered velocity. This results in a wall model that requires only the solution of algebraic equations. While the above-mentioned models all consistently include

† Department of Mechanical and Production Engineering, Aarhus University, Denmark
‡ Department of Mechanical Engineering, Pennsylvania State University

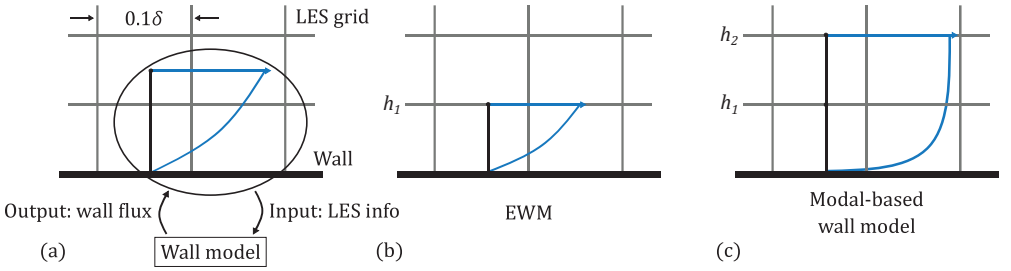

FIGURE 1. Schematics of (a) WMLES, (b) the EWM, where the wall model and the LES match at the first off-wall grid point, and (c) a modal-based wall model where the LoW is augmented by an additional term and the wall model and the LES match at two off-wall grid points.

non-equilibrium effects, they also share a common weakness. Specifically, they rely on a mixing-length closure for the eddy viscosity in the TBLEs, which is only accurate in equilibrium conditions. Another interesting wall modeling approach is the dynamic slip wall model (Bose & Moin 2014; Bae *et al.* 2019). In this approach, a slip boundary condition is derived from the filtered Navier–Stokes equations, which is then used instead of the traditional Neumann boundary condition at the wall. While this approach is promising, the dynamic slip wall model has been found to be sensitive to sub-grid scale (SGS) modeling and numerical filtering operations (Bae *et al.* 2019).

In this brief, we focus on a different class of wall models that we refer to as modal-based wall models. The idea is to augment the LoW such that the ansatz used for velocity reconstruction in the wall-adjacent cell(s) provides a more realistic description of the near-wall velocity profile than the LoW. In algebraic EWMs, the following ansatz is used for the near-wall flow

$$\mathbf{U} = \mathbf{c}\mathrm{LoW}(h^+), \tag{1.1}$$

where $\mathbf{c} = (c_x, c_y, c_z)$ is a coefficient vector and $\mathbf{U} = (U, V, W)$ are the streamwise, spanwise, and vertical velocity components (in the global coordinate system) at a height h from the wall as shown in Figure 1. Here, $\mathrm{LoW}(h^+)$ is usually taken to be the logarithmic law of the wall (Prandtl 1925; Kármán 1930), $h^+ = (u_\tau/\nu)h$ is the wall-unit-scaled height from the wall, ν is the kinematic viscosity, $u_\tau = \sqrt{\tau_w/\rho}$ is the friction velocity, τ_w is the wall shear stress magnitude, and ρ is the fluid density. We take $\mathrm{LoW}(h^+)$ to include the viscous sublayer, the buffer layer, and the logarithmic layer, but not the wake layer. Further, $\mathrm{LoW}(h^+)$ is renormalized to absorb the friction velocity into the coefficients. We generalize these EWMs models by using the augmented ansatz

$$\mathbf{U} = \mathbf{c}_1\mathrm{LoW}(h^+) + \mathbf{c}_2 g(h^+), \tag{1.2}$$

where $g(h^+)$ is, at this point, a generic nondimensional function. Figure 1(b,c) are schematics of the velocity reconstruction according to Eqs. (1.1) and (1.2), respectively. Inclusion of the function g gives the wall model in Figure 1(c) the ability to account for deviations from the LoW scaling, and thus, to respond to both instantaneous fluctuations and non-equilibrium effects. Monkewitz & Nagib (2023) argued that $g \sim h$ to leading order, a choice that has been used in previous wall modeling efforts (Yang *et al.* 2015; Lv *et al.* 2021). However, other choices that more closely mimic the instantaneous physics of wall-bounded turbulent flows could yield better results.

We recently explored the above-referenced modal-based approach to wall modeling in (Hansen *et al.* 2023). We also note that similar efforts are under investigation by Piomelli

et al. (2023). In Hansen *et al.* (2023), several different modes g were investigated. This includes a linear mode $g \sim h$, similar to Yang *et al.* (2015) and Lv *et al.* (2021), which we refer to as the linear wall model (LINWM). Another mode, based on the root-mean-square (rms) profile from a $Re_\tau = 5200$ turbulent channel, we refer to as the rms wall model (RMSWM). Here, $Re_\tau = u_\tau \delta/\nu$ is the friction Reynolds number with δ the half-channel height or boundary layer thickness. Finally, a mode determined based on modal analysis of the near-wall region of a 2D turbulent channel was considered. This latter g mode was found using the proper orthogonal decomposition (POD). This choice was motivated by the physical underpinning of POD, specifically, that POD modes capture more turbulent kinetic energy than any other orthogonal basis (Berkooz *et al.* 1993). The wall model based on this mode is referred to as the POD-mode-augmented wall model (PODWM). These wall models were applied to channel flows subjected to strong adverse pressure gradients and moderate transverse pressure gradients. In both cases, the PODWM performed significantly better than the EWM, LINWM, and RMSWM. It was further observed that the LINWM showed slight improvements compared to the EWM, while the RMSWM generally had the worst performance of all the models. For this reason, the RMSWM is not considered in this brief. Further details on these results can be found in Hansen *et al.* (2023). While these results are encouraging, the usefulness of these models (or lack thereof) in more challenging configurations remains to be tested. Specifically, the utility of the POD-based g mode in cases with complex geometries and flow separation is far from obvious, given that it is obtained from an equilibrium channel flow, and deserves further investigation. This brief aims to address these questions by performing a comparative WMLES study of the Gaussian bump case using the EWM, LINWM, and PODWM.

The remainder of this brief is organized as follows. In Section 2, we provide further details on the modal-based wall model formulation. In Section 3, we present WMLES results for a turbulent channel flow and the Gaussian bump case using the different modal-based wall models. Finally, in Section 4, we provide some concluding remarks.

2. Methodology

2.1. *Wall model formalism*

We start by considering algebraic EWMs to provide some context for the LINWM and PODWM. In these models, we employ the LoW ansatz in Eq. (1.1) as an approximation of the near-wall flow. This is done by matching the LoW locally with the LES velocity components. As Eq. (1.1) has only one mode, i.e., the LoW mode, we can determine the coefficients $\mathbf{c} = (c_x, c_y, c_z)$ from matching information at a single off-wall location. This gives the equations

$$c_x \mathrm{LoW}(h^+) = U, \quad c_y \mathrm{LoW}(h^+) = V, \quad c_z \mathrm{LoW}(h^+) = W, \tag{2.1}$$

where h^+ is the wall-unit-scaled height of the matching location and U, V, and W are the streamwise, spanwise, and vertical LES velocity components (in the global coordinate system) at this height. Note that unlike the original formulation in Hansen *et al.* (2023), we have chosen to include all three velocity components. This is done because fluxes for all velocity components must be specified at the wall for WMLES using a finite volume code. This is in contrast to codes that use the finite difference method along the wall-normal direction, in which case the no penetration boundary condition can be used for the wall-normal velocity component, and wall stress boundary conditions are used only

for the wall-parallel velocities. When the coefficients in Eq. (2.1) are determined, we can then calculate the wall shear stress $\boldsymbol{\tau}_w = (\tau_x, \tau_y, \tau_z)$ from Eq. (1.1) as follows

$$\boldsymbol{\tau}_w = \nu \left.\frac{d\mathbf{U}}{dh}\right|_{h=0} = \nu \mathbf{c} \left.\frac{d\mathrm{LoW}}{dh^+}\right|_{h=0} \left.\frac{dh^+}{dh}\right|_{h=0} = \mathbf{c} u_\tau, \tag{2.2}$$

where we have used that $dh^+/dh = u_\tau/\nu$ and $d\mathrm{LoW}/dh^+|_{h=0} = 1$ by definition. To relate the friction velocity u_τ to the coefficients $\mathbf{c}$, we note that EWMs assume a local state of equilibrium. Therefore, the wall shear stress amplitude is given by $\tau_w = |\boldsymbol{\tau}_w| = u_\tau^2$. This, together with Eq. (2.2), gives the following relation

$$u_\tau = (c_x^2 + c_y^2 + c_z^2)^{1/2}. \tag{2.3}$$

Thus, the appearance of the friction velocity in Eq. (2.1) (contained in h^+) results in this being a nonlinear set of equations that would require an iterative method to obtain the exact solution. However, this requirement can be removed by using u_τ from the previous time step. In this case, Eq. (2.1) can be solved directly, reducing the computational cost of the wall model, and Eq. (2.2) is then invoked to calculate the wall shear stress.

The proposed extension in Eq. (1.2), on the other hand, has two modes, i.e., LoW and g. To determine the coefficients $\mathbf{c}_1 = (c_{1x}, c_{1y}, c_{1z})$ and $\mathbf{c}_2 = (c_{2x}, c_{y2}, c_{2z})$, matching with the LES at two off-wall locations is used

$$\begin{aligned}
c_{1x}\mathrm{LoW}(h_1^+) + c_{2x} g(h_1^+) &= U_1, \qquad & c_{1x}\mathrm{LoW}(h_2^+) + c_{2x} g(h_2^+) &= U_2, \\
c_{1y}\mathrm{LoW}(h_1^+) + c_{2y} g(h_1^+) &= V_1, \qquad & c_{1y}\mathrm{LoW}(h_2^+) + c_{2y} g(h_2^+) &= V_2, \\
c_{1z}\mathrm{LoW}(h_1^+) + c_{2z} g(h_1^+) &= W_1, \qquad & c_{1z}\mathrm{LoW}(h_2^+) + c_{2z} g(h_2^+) &= W_2.
\end{aligned} \tag{2.4}$$

Here, h_1^+ and h_2^+ are the wall-unit-scaled heights of the two matching locations, and $U_{1,2}$, $V_{1,2}$, and $W_{1,2}$ are the streamwise, spanwise, and vertical LES velocity components (in the global coordinate system) at these heights. The wall shear stress $\boldsymbol{\tau}_w = (\tau_x, \tau_y, \tau_z)$ can then be calculated similar to the EWM as

$$\boldsymbol{\tau}_w = \nu \left.\frac{d\mathbf{U}}{dh}\right|_{h=0} = \nu \left(\mathbf{c}_1 \left.\frac{d\mathrm{LoW}}{dh^+}\right|_{h=0} + \mathbf{c}_2 \left.\frac{dg}{dh^+}\right|_{h=0} \right) \left.\frac{dh^+}{dh}\right|_{h=0} = (\mathbf{c}_1 + \mathbf{c}_2) u_\tau, \tag{2.5}$$

where we have again used that $dh^+/dh = u_\tau/\nu$ and $d\mathrm{LoW}/dh^+|_{h=0} = 1$, while we enforce $dg/dh^+|_{h=0} = 1$ through normalization of g. Further, as for EWMs, we assume that the wall shear stress magnitude can be expressed through a local friction velocity such that $\tau_w = |\boldsymbol{\tau}_{\boldsymbol{w}}| = u_\tau^2$ still holds for the proposed model. Using this assumption, together with Eq. (2.5), we get

$$u_\tau = \left[(c_{1x} + c_{2x})^2 + (c_{1y} + c_{2y})^2 + (c_{1z} + c_{2z})^2 \right]^{1/2}. \tag{2.6}$$

Comparing with the EWM result from Eq. (2.3), we see that the structure is very similar. Further, the friction velocity u_τ in Eq. (2.4) (contained in h_1^+, h_2^+) results in a set of nonlinear equations, which can be handled in the same way as for the EWM. With the coefficients determined, Eq. (2.5) is then invoked to compute the wall shear stress. It is worth noting that the model reduces to an algebraic EWM when $\mathbf{c}_2 = 0$.

In our original implementation of the EWM, LINWM, and PODWM from Hansen *et al.* (2023) in the LESGO solver, we followed the approach from Yang *et al.* (2017), where additional filtration is applied to the velocities at the matching location(s) to remove log-layer mismatch. However, as reported in Goc *et al.* (2020), this treatment has been found to be unnecessary for WMLES with the charLES solver when the EWM and

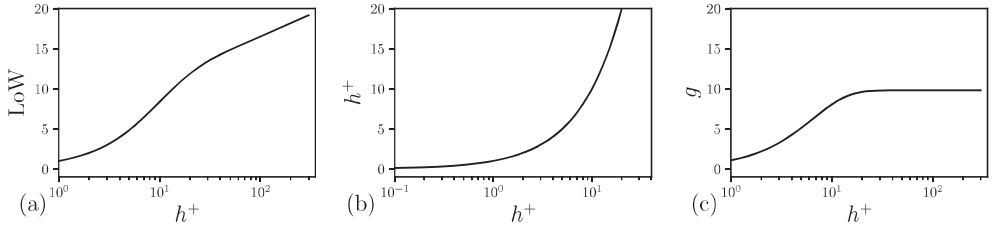

FIGURE 2. Modes used in the different wall models: (a) the LoW mode from Eq. (2.8), (b) the linear mode given by h^+, and (c) the POD-based g mode from Eq. (2.9).

hexagonal close-packed (HCP) grids are used (we also use HPC grids for the WMLES results presented in this brief). Nonetheless, as we discuss in Section 3.2, this additional filtering is found to be important for the PODWM. As we consider unstructured grids in this brief, temporal filtering is used given the complexity of constructing spatial filtering operators in this case. Specifically, we chose to use an exponential time filter (Yang *et al.* 2015, 2017) given by

$$\bar{f}_{t+1} = a\bar{f}_t + (1-a)f_t, \tag{2.7}$$

where f is the variable being filtered, $\bar{f}$ is the time filtered variable, and $0 \leq a \leq 1$ is the filtering constant. The determination of an appropriate filtering constant is considered in Section 3.2.

2.2. *Wall model modes*

We now describe the modes used in the EWM, LINWM, and PODWM. For brevity, we refer to Hansen *et al.* (2023) for details on the construction of the POD-based g mode. Figure 2(a) shows the LoW mode used in the EWM which is based on the mean velocity profile from a direct numerical simulation (DNS) of turbulent channel flow at $Re_\tau = 5200$ (Lee & Moser 2015). The behavior of the LoW mode conforms to $U^+ = \log(h^+)/\kappa + B$ at sufficiently large h^+ where $\kappa = 0.41$ is the von Kármán constant and $B = 5.2$. An analytical expression of the LoW mode is obtained from Reichardt (1951)

$$\mathrm{LoW}(h^+) = \frac{1}{\kappa}\ln(1+kh^+) + A_1\left[1 - \exp\left(-\frac{h^+}{A_2}\right) - \left(\frac{h^+}{A_2}\right)\exp\left(-A_3h^+\right)\right]. \tag{2.8}$$

We have recalibrated the constants A_1, A_2, and A_3 by fitting the expression in Eq. (2.8) to the mean velocity profile from a $Re_\tau = 5200$ channel over the interval $0 \leq h^+ \leq 1000$. The resulting values are $A_1 = 7.4$, $A_2 = 9.5$, and $A_3 = 0.29$. Figure 2(b) shows the linear mode given by h^+ which is used in the LINWM. Finally, Figure 2(c) shows the POD-based mode g. The mode is approximately constant away from the wall and conforms to the no-slip condition at the wall. We have found an analytical expression for this mode by fitting a functional form that is similar to the second part of Eq. (2.8) to the g mode in Figure 2(c), also over the interval $0 \leq h^+ \leq 1000$. The resulting expression is given by

$$g(h^+) = B_1\left[1 - \exp\left(-\frac{h^+}{B_2}\right) - \left(\frac{h^+}{B_3}\right)\exp\left(-B_4h^+\right)\right], \tag{2.9}$$

and the values of the constants are $B_1 = 9.8$, $B_2 = 3.6$, $B_3 = 5.7$, and $B_4 = 0.27$.

A basic requirement of a wall model is that it conforms to the no-slip condition in the wall-resolved limit. Here, we discuss the behavior of the LINWM and PODWM when

the viscous sublayer is resolved. In this case, we have

$$\mathbf{U} = \left.\frac{d\mathbf{U}}{dh}\right|_{h=0} h, \tag{2.10}$$

at first off-wall grid points. We note that the LoW mode, the g mode, and, obviously, the linear mode are all linear functions of h^+ in the viscous sublayer. Therefore, in the wall-resolved case, we have

$$\text{LoW} = g = h^+. \tag{2.11}$$

It follows from Eqs. (2.10) and (2.11) that Eq. (2.4) reduces to

$$(\mathbf{c}_1 + \mathbf{c}_2)h_1^+ = \left.\frac{d\mathbf{U}}{dh}\right|_{h=0} h_1, \qquad (\mathbf{c}_1 + \mathbf{c}_2)h_2^+ = \left.\frac{d\mathbf{U}}{dh}\right|_{h=0} h_2. \tag{2.12}$$

The two equations have the following solution

$$\mathbf{c}_1 + \mathbf{c}_2 = \frac{\mathbf{U}}{|\mathbf{U}|} u_\tau. \tag{2.13}$$

We see that, although $\mathbf{c}_1$ and $\mathbf{c}_2$ are not uniquely determined, $\mathbf{c}_1 + \mathbf{c}_2$ is. As a result, the wall shear stress will also be uniquely determined. We also notice that Eq. (2.13) is non-singular even when the wall shear stress is 0. Hence, $\tau_w = 0$ is a removable singularity ($\tau_w = 0$ is a singularity because h^+ is not defined when $\tau_w = 0$; it is removable because it does not create any mathematical singularity to the calculation of the wall shear stress). In terms of numerical implementation, one option would be to do a minimum norm solution. We have chosen to add a simple if statement that allows the code to treat wall-resolved grids separately.

3. Wall-modeled LES results

We first give some background on the charLES solver used for the WMLES in Section 3.1. Next, we consider WMLES results of a turbulent channel flow at $Re_\tau = 1000$ in Section 3.2. This case serves as a sanity check for the wall model implementations in the charLES solver. Further, it is used to determine an appropriate filtering constant for the exponential time filter discussed in Section 2.1. Following this, we consider the WMLES results for the Gaussian bump case in Section 3.3.

3.1. *Numerical solver*

The charLES solver is an unstructured finite volume code that solves the filtered compressible Navier–Stokes equations. The solver is formally second-order accurate in space and uses explicit time stepping by a third-order accurate Runge–Kutta method. Further details on the solver and validation cases can be found in Bres *et al.* (2018) and Goc *et al.* (2021).

3.2. *Turbulent channel flow*

We present WMLES results for a turbulent channel flow at $Re_\tau = 1000$ using the EWM, LINWM, and PODWM. The simulation details for this case are given in Table 1. We note that the EWM matches with the LES using the LES velocities at the first off-wall cell center, while both the LINWM and PODWM match using the LES velocities at the first and second off-wall cell centers. Further, regarding SGS modeling, we use the dynamic Smagorinsky model (DSM) (Germano *et al.* 1991; Lilly 1992).

Re_τ	Grid	Domain	Δh^+	CFL
1000	$64 \times 24 \times 32$	$2\pi \times 2 \times \sqrt{3}\pi/2$	47	≤ 3

TABLE 1. WMLES details for the channel case. The half-channel height δ is used to normalize the numbers in the Domain column. Here, Δh is the height of the first off-wall cell center.

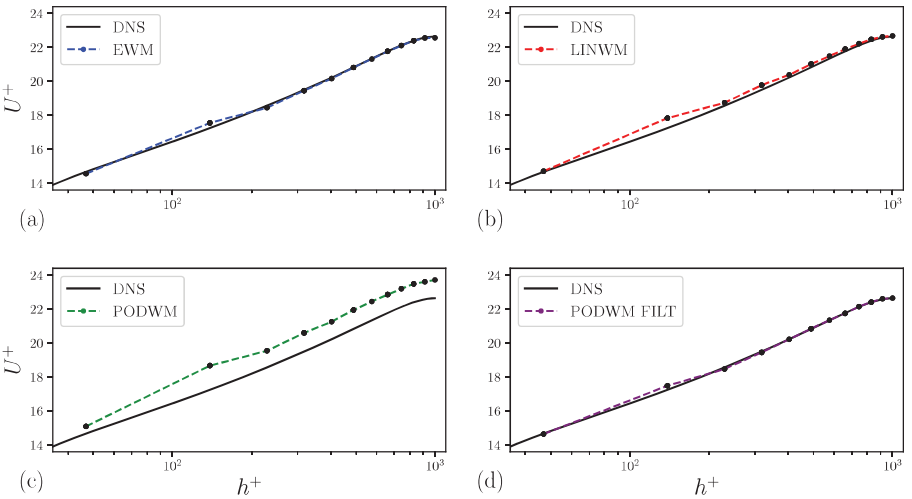

FIGURE 3. WMLES results in a $Re_\tau = 1000$ turbulent channel using the different wall models: (a) the EWM, (b) the LINWM, (c) the PODWM without filtering, and (d) the PODWM using the filtering constant $a = 0.99$.

The mean velocity profiles from WMLES using the EWM, LINWM, and PODWM (with and without filtering) are shown in Figure 3. We observe the following. Firstly, for the EWM results shown in Figure 3(a), we see that the EWM gives good predictions for the mean velocity profile without any filtering of the input velocities. Secondly, for the LINWM results shown in Figure 3(b), we again see a good agreement for the mean velocity profile. Similar to the EWM, no filtering of the input velocities is needed in this case. Thirdly, we focus on the PODWM results without filtering shown in 3(c). We observe that the PODWM gives a poor prediction of the mean velocity profile when no additional filtering is applied. Finally, we consider the PODWM results with filtering shown in 3(d). We see that the PODWM shows a good agreement with the mean velocity profile when using a filtering constant of $a = 0.99$.

While not shown here, we note that the EWM and LINWM also give good results in turbulent channel flow at $Re_\tau = 5200$ without any filtering of the LES velocities at the matching location(s). Further, the PODWM with the same filtering constant of $a = 0.99$ gives good results for the $Re_\tau = 5200$ channel as well. While this is encouraging, the filtering constant nonetheless remains a free parameter in the PODWM, which is generally undesirable. A more attractive approach would be to determine the filtering constant using a dynamic procedure based on local flow quantities. However, we choose to leave this possibility for future investigations.

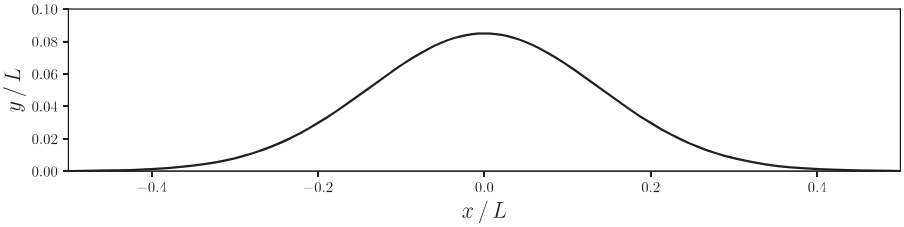

FIGURE 4. Plot of the Gaussian bump geometry.

Cases	Re_L	# Control volumes	Domain	Δh^+	CFL
Coarse	2×10^6	3.5×10^6	$3.5 \times 1.0 \times 0.08$	$[15, 79]$	≤ 3
Medium	2×10^6	12.8×10^6	$3.5 \times 1.0 \times 0.08$	$[9, 42]$	≤ 3
Fine	2×10^6	52.2×10^6	$3.5 \times 1.0 \times 0.08$	$[4, 21]$	≤ 3

TABLE 2. WMLES details for Gaussian bump cases. The spanwise width of the speed bump experiment L is used to normalize the numbers in the Domain column. Here, Δh is the height of the first off-wall cell center and the normalization to inner units is by the EWM results.

3.3. *Gaussian bump*

The three-dimensional speed bump experiment was developed jointly by Boeing and the Williams group at the University of Washington (Williams *et al.* 2020). Uzun & Malik (2022) performed a quasi-DNS of the simplified, two-dimensional, spanwise periodic variant of this geometry, which we will take as the ground truth for comparison with the WMLES results. The profile of the Gaussian bump is given by the following function

$$H(x) = \frac{H_0}{2} e^{-(x/x_0)^2}, \tag{3.1}$$

and corresponds to the streamwise profile along the spanwise centerline of the speed bump experiment in Williams *et al.* (2020). Here, $H_0 = 0.085L$ is the peak height of the bump, and $x_0 = 0.195L$ controls the streamwise extent of the bump. The Reynolds number for the flow Re_L is defined in terms of the upstream freestream velocity U_∞ and the spanwise width of the speed bump experiment L. A plot of the Gaussian bump geometry is shown in Figure 4. Some details of the simulation setup are given in Table 2. Further details on the WMLES setup can be found in Whitmore *et al.* (2021) and Agrawal *et al.* (2022). In regard to additional filtering of the velocities at the matching locations(s), we apply no filtering for the EWM and LINWM, while we apply filtering with a filtering constant of $a = 0.99$ for the PODWM. Further, the matching location(s) for the EWM, LINWM, and PODWM are the same as in the turbulent channel flow case in Section 3.2, and we again use the DSM as the SGS model. Finally, we define the quantities of interest for this flow, which are the friction and pressure coefficients

$$C_f = \frac{\tau_w}{1/2\rho_\infty U_\infty^2}, \qquad C_p = \frac{p - p_{\text{ref}}}{1/2\rho_\infty U_\infty^2}. \tag{3.2}$$

Here, τ_w is the mean wall shear stress, p is the mean wall pressure, and p_{ref} is a reference pressure. Following Williams *et al.* (2020), p_{ref} is taken as the mean wall pressure at the upstream location $x/L = -0.83$.

Moving on to the results, we first consider the results on the coarse grid, which are shown in Figure 5. From Figure 5(a), we see that the EWM and LINWM give similar

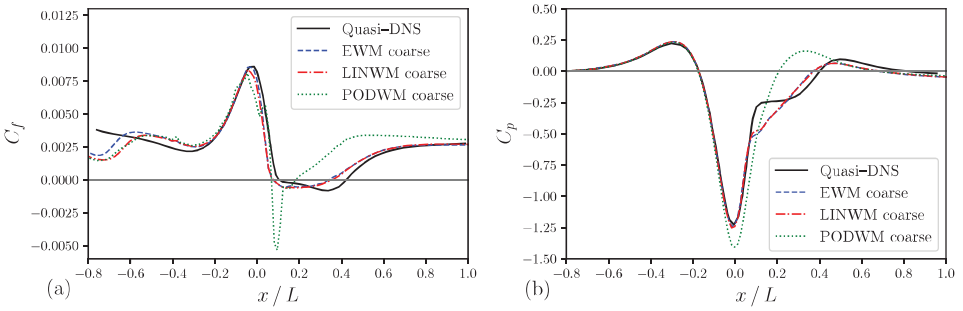

FIGURE 5. WMLES results on the Gaussian bump using the coarse grid for the EWM, LINWM, and PODWM: (a) friction coefficient C_f and (b) pressure coefficient C_p. The quasi-DNS results shown in black are from Uzun & Malik (2022).

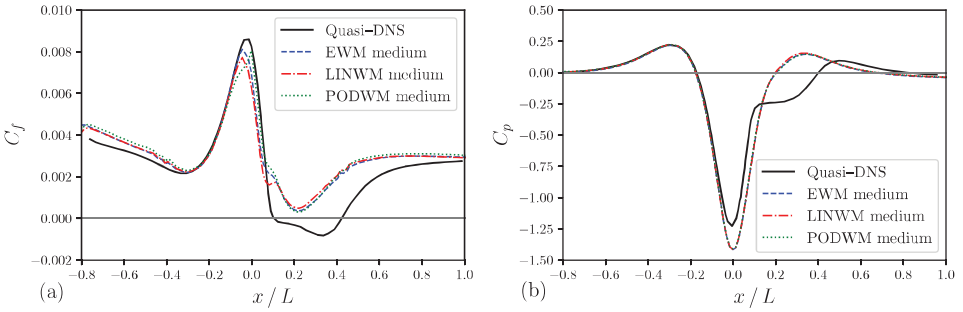

FIGURE 6. WMLES results on the Gaussian bump using the medium grid for the EWM, LINWM, and PODWM: (a) friction coefficient C_f and (b) pressure coefficient C_p. The quasi-DNS results shown in black are from Uzun & Malik (2022).

results for C_f. The PODWM, on the other hand, performs significantly worse than the other models in this case. Specifically, the PODWM produces a large negative spike in C_f around $x/L \approx 0.09$. We will provide further explanation of why this spike occurs at the end of this section. We also note that deviation in C_f from the quasi-DNS results seen at the inlet is due to the application of a uniform velocity inflow boundary condition for the WMLES as opposed to the recycling and rescaling boundary condition used in Uzun & Malik (2022). From Figure 5(b), we see that the trends observed for C_f are also true for C_p. That is, the EWM and LINWM give similar results, while the PODWM has the worst performance. Still, contrary to the results for C_f, the PODWM results for C_p do not show a drastic spike.

Next, we examine the results on the medium grid shown in Figure 6. In Figure 6(a), we see that overall the different wall models give much more similar results than on the coarse grid. Still, for the LINWM and PODWM, we see that they show some difference compared to the EWM around $-0.1 \leq x/L \leq 0.1$. Another significant observation is that the spike in C_f predicted by the PODWM on the coarse grid is no longer present in this case. From Figure 6(b), we observe that no significant difference between the different models can be seen in the C_p predictions. It is also important to mention that the results on the medium grid in Figure 6 are generally worse than the coarse grid case in Figure 5 and that none of the models separate in the medium grid case. This problem

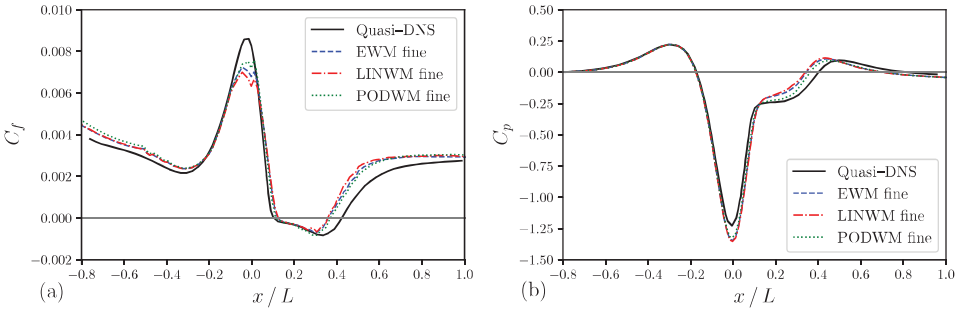

FIGURE 7. WMLES results on the Gaussian bump using the fine grid for the EWM, LINWM, and PODWM: (a) friction coefficient C_f and (b) pressure coefficient C_p. The quasi-DNS results shown in black are from Uzun & Malik (2022).

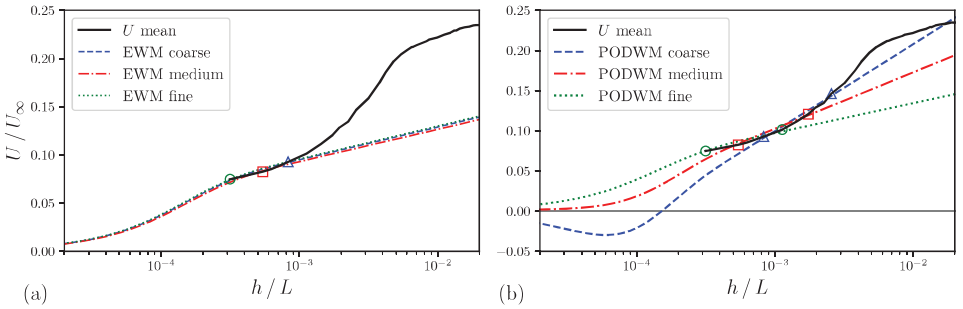

FIGURE 8. Effect of different coupling points on the mean streamwise velocity at $x/L = 0.9$: (a) EWM results and (b) PODWM results. Here, U mean is the mean streamwise velocity from the PODWM on the fine grid, and h is the wall-normal distance from the bump surface at $x/L = 0.9$.

of non-monotonic convergence has also been observed in previous works (Agrawal *et al.* 2022).

The results on the fine grid are shown in Figure 7. From Figure 7(a), we see that all of the models have very similar performance in predicting C_f for this case. We also observe that all of the models do a reasonable job of capturing the separation bubble. However, it should be mentioned that all the models underpredict the peak in C_f compared to the results on the coarse and medium grids. This is consistent with the results in Agrawal *et al.* (2022), where it is demonstrated that this underprediction can be alleviated by improvements in SGS modeling. For the C_p predictions in Figure 7(b), we also see similar performance for the different models and that the results are improved compared to the coarse and medium grid cases.

Finally, we provide an explanation for the peak in the C_f predictions of the PODWM on the coarse grid seen in Figure 5(a). To do this, we have extracted time series of each velocity component from the PODWM simulations on the fine grid for points along a line that is normal to the bump surface at $x/L = 0.09$. These velocity time series are then used to calculate time series of the EWM and PODWM coefficients in Eqs. (2.1) and (2.4), respectively. We then use these coefficient time series to calculate the average streamwise velocity profiles predicted by the EWM and PODWM. These are shown in Figure 8. From Figure 8(a), we see that the EWM consistently produces mean streamwise

velocity profiles with a positive wall shear stress. This is consistent with the EWM results on all of the grids as seen in panel (a) of Figures 5-7. As seen from Figure 8(b), this is not the case for the PODWM, which produces a separated mean streamwise velocity profile for the two matching locations that are consistent with the coarse grid. Specifically, we observe that $\langle c_{1x} \rangle = 0.019$ and $\langle c_{2x} \rangle = -0.024$ for this case. Therefore, the g mode is causing a large downward shift in the log-law behavior far from the wall, which then results in a separated flow in the near-wall region.

4. Conclusions

In this brief, we have presented WMLES results for the Gaussian bump case using three different wall models: the EWM, LINWM, and PODWM. The EWM is an algebraic equilibrium wall model, while the LINWM and PODWM are both modal-based wall models that augment the LoW by an additional term, i.e., a linear function h^+ and the POD-based mode $g(h^+)$, respectively.

The results for the LINWM show that augmenting the LoW by a linear function does not improve the results compared to the EWM. This shows that the additional linear mode does not significantly alter the wall shear stress predictions produced by the EWM. The PODWM results show that the POD-based g mode can respond very aggressively, leading to a large nonphysical spike in C_f as observed on the coarse grid. We also observed that this spike in C_f disappears with better grid resolution and that the PODWM performs similarly to the EWM on the medium and fine grids. Finally, we proposed some explanations for these observations.

Acknowledgments

C.H. and M.A. acknowledge the financial support from the Independent Research Fund Denmark (DFF) under Grant No. 1051-00015B. C.H. further acknowledges the financial support of the Fulbright scholarship program in connection with his stay at CTR. X.Y. acknowledges the financial support from the Office of Naval Research under contract N000142012315. Finally, the authors acknowledge Michael Whitmore and Rahul Agrawal for fruitful discussions and help with the implementation of the modal-based wall models in the charLES solver.

REFERENCES

Agrawal, R., Whitmore, M. P., Griffin, K. P., Bose, S. T. & Moin, P. 2022 Non-Boussinesq subgrid-scale model with dynamic tensorial coefficients. *Phys. Rev. Fluids* **7**, 074602.

Bae, H. J., Lozano-Durán, A., Bose, S. T. & Moin, P. 2019 Dynamic slip wall model for large-eddy simulation. *J. Fluid Mech.* **859**, 400–432.

Berkooz, G., Holmes, P. & Lumley, J. L. 1993 The proper orthogonal decomposition in the analysis of turbulent flows. *Annu. Rev. Fluid Mech.* **25**, 539–575.

Bose, S. T. & Moin, P. 2014 A dynamic slip boundary condition for wall-modeled large-eddy simulation. *Phys. Fluids* **26**, 015104.

Bose, S. T. & Park, G. I. 2018 Wall-modeled large-eddy simulation for complex turbulent flows. *Annu. Rev. Fluid Mech.* **50**, 535–561.

Bou-Zeid, E., Meneveau, C. & Parlange, M. 2005 A scale-dependent Lagrangian

dynamic model for large eddy simulation of complex turbulent flows. *Phys. Fluids* **17**, 025105.

Bres, G. A., Bose, S. T., Emory, M., Ham, F. E., Schmidt, O. T., Rigas, G. & Colonius, T. 2018 Large-eddy simulations of co-annular turbulent jet using a Voronoi-based mesh generation framework. *AIAA Paper* 2018-3302.

Chen, P. E., Lv, Y., Xu, H. H., Shi, Y. & Yang, X. I. A. 2022 LES wall modeling for heat transfer at high speeds. *Phys. Rev. Fluids* **7**, 014608.

Choi, H. & Moin, P. 2012 Grid-point requirements for large eddy simulation: Chapman's estimates revisited. *Phys. Fluids* **24**, 011702.

De Vanna, F., Cogo, M., Bernardini, M., Picano, F. & Benini, E. 2021 Unified wall-resolved and wall-modeled method for large-eddy simulations of compressible wall-bounded flows. *Phys. Rev. Fluids* **6**, 034614.

Fowler, M., Zaki, T. A. & Meneveau, C. 2022 A Lagrangian relaxation towards equilibrium wall model for large eddy simulation. *J. Fluid Mech.* **934**, A44.

Germano, M., Piomelli, U., Moin, P. & Cabot, W. H. 1991 A dynamic subgrid-scale eddy viscosity model. *Phys. Fluids A* **3**, 1760–1765.

Goc, K., Bose, S. T. & Moin, P. 2020 Subgrid-scale modeling sensitivities in wall-modeled large-eddy simulations of a high-lift aircraft configuration. *Annual Research Briefs,* Center for Turbulence Research, Stanford University, pp. 49–58.

Goc, K. A., Lehmkuhl, O., Park, G. I., Bose, S. T. & Moin, P. 2021 Large eddy simulation of aircraft at affordable cost: a milestone in computational fluid dynamics. *Flow* **1**, E14.

Hansen, C., Yang, X. I. A. & Abkar, M. 2023 A POD-mode-augmented wall model and its applications to flows at non-equilibrium conditions. *J. Fluid Mech.* **975**, A24.

Kármán, V. T. 1930 Mechanical similarity and turbulence. In *Proc. 3rd Int. Cong. Appl. Mech., Stockholm, Sweden*, pp. 85–92.

Kawai, S. & Larsson, J. 2012 Wall-modeling in large eddy simulation: length scales, grid resolution, and accuracy. *Phys. Fluids* **24**, 015105.

Larsson, J., Kawai, S., Bodart, J. & Bermejo-Moreno, I. 2016 Large eddy simulation with modeled wall-stress: recent progress and future directions. *Mech. Eng. Rev.* **3**, 15–00418.

Lee, M. & Moser, R. D. 2015 Direct numerical simulation of turbulent channel flow up to $\mathrm{Re}_\tau \approx 5200$. *J. Fluid Mech.* **774**, 395–415.

Lilly, D. K. 1992 A proposed modification of the Germano subgrid-scale closure method. *Phys. Fluids A* **4**, 633–635.

Lv, Y., Huang, X. L. D., Yang, X. & Yang, X. I. A. 2021 Wall-model integrated computational framework for large-eddy simulations of wall-bounded flows. *Phys. Fluids* **33**, 125120.

Monkewitz, P. A. & Nagib, H. M. 2023 The hunt for the Kármán 'constant' revisited. *J. Fluid Mech.* **967**, A15.

Park, G. I. & Moin, P. 2014 An improved dynamic non-equilibrium wall-model for large eddy simulation. *Phys. Fluids* **26**, 015108.

Park, G. I. & Moin, P. 2016 Numerical aspects and implementation of a two-layer zonal wall model for LES of compressible turbulent flows on unstructured meshes. *J. Comput. Phys.* **305**, 589–603.

Piomelli, U. & Balaras, E. 2002 Wall-layer models for large-eddy simulations. *Annu. Rev. Fluid Mech.* **34**, 349–374.

Piomelli, U., Hantsis, Z., Chan, M. & McKeon, B. 2023 Resolvent modes as the foundation for LES wall models. In *Bull. Am. Phys. Soc*, Abstract: J12.00003.

Prandtl, L. 1925 Bericht über untersuchungen zur ausgebildeten turbulenz. *J. Appl. Math. Mech.* **5**, 136–139.

Reichardt, H. 1951 Vollständige darstellung der turbulenten geschwindigkeitsverteilung in glatten leitungen. *J. Appl. Math. Mech.* **31**, 208–219.

Schumann, U. 1975 Subgrid scale model for finite difference simulations of turbulent flows in plane channels and annuli. *J. Comput. Phys.* **18**, 376–404.

Uzun, A. & Malik, M. R. 2022 High-fidelity simulation of turbulent flow past Gaussian bump. *AIAA J.* **60**, 2130–2149.

Whitmore, M., Griffin, K., Bose, S. & Moin, P. 2021 Large-eddy simulation of a Gaussian bump with slip-wall boundary conditions. *Annual Research Briefs,* Center for Turbulence Research, Stanford University, pp. 45–58.

Williams, O., Samuell, M., Sarwas, E. S., Robbins, M. & Ferrante, A. 2020 Experimental study of a CFD validation test case for turbulent separated flows. *AIAA Paper* 2020-0092.

Yang, X. I. A. & Griffin, K. P. 2021 Grid-point and time-step requirements for direct numerical simulation and large-eddy simulation. *Phys. Fluids* **33**, 015108.

Yang, X. I. A. & Lv, Y. 2018 A semi-locally scaled eddy viscosity formulation for LES wall models and flows at high speeds. *Theor. Comput. Fluid Dyn.* **32**, 617–627.

Yang, X. I. A., Park, G. I. & Moin, P. 2017 Log-layer mismatch and modeling of the fluctuating wall stress in wall-modeled large-eddy simulations. *Phys. Rev. Fluids* **2**, 104601.

Yang, X. I. A., Sadique, J., Mittal, R. & Meneveau, C. 2015 Integral wall model for large eddy simulations of wall-bounded turbulent flows. *Phys. Fluids* **27**, 025112.